ARTICLE

Efficient and Semi-Transparent Perovskite Solar Cells Using a Room-Temperature Processed MoOx/ITO/Ag/ITO Electrode

Received 00th January 20xx,
Accepted 00th January 20xx

DOI: 10.1039/x0xx00000x

Zhengfei Wei*[a], Benjamin Smith[a], Francesca De Rossi[a], Justin Searle[a], David A. Worsley[a] and Trystan M. Watson*[a]

In order to achieve semi-transparency in perovskite solar cells, the electrode materials must be as transparent as possible. In this work, MoO_x/ITO/Ag/ITO (MoO_x/IAI) thin films with high average transmittance of 79.90% between 400 nm and 900 nm were introduced as the top transparent electrode to explore its influences on optoelectronic properties of the fabricated perovskite solar cells. MoO_x has been demonstrated previously as protection from sputtering damage using a conventional ITO top electrode, however it is shown here to provide protection from a sputtered IAI film that provides superior transparency and conductivity and is deposited using more favourable low temperature processing conditions. MoO_x and Ag were thermally evaporated and ITO was radio-frequency magnetron sputtered at room temperature. The resulting semi-transparent solar cells showed power conversion efficiency of 12.85% (steady-state efficiency of 11.3%) along with a much-reduced degradation rate as compared to the reference device with only a Ag top electrode. With such a combination of performance and transparency, this work shows great promise in application of perovskite solar cells into window glazing products for building integrated photovoltaic applications (BIPV), powering internet of things (IoT) and combining into tandem solar cells with industrially mature photovoltaic technologies such as silicon and copper indium gallium di-selenide (CIGS).

Introduction

The organic-inorganic lead halide perovskite solar cell is the fastest growing photovoltaic research area with certified efficiencies for small area devices reaching over 23% in the last few years.[1] Tuneable bandgap, high absorption and long diffusion lengths make this material especially attractive for application as a semi-transparent solar cell.[2] In order to extend its application into either single junction window products or into tandem devices with Silicon technology, a highly transparent and conductive top electrode is required. Previously, solution processed silver nanowires,[3-5] carbon nanotubes,[6] and PEDOT:PSS[7] have been demonstrated, however these electrode options generally suffer poor long-term operational stability and demonstrate high efficiency that is difficult to reproduce. Laminated graphene[8] or Ni-mesh[9] top electrodes have been successfully demonstrated; however these devices are hindered by strong hysteresis or reproducibility issues. Vacuum sputtered transparent conductive oxides (TCO) such as indium tin oxide (ITO)[2, 10-13], hydrogenated indium oxide (In_2O_3:H)[14] aluminium doped zinc oxide (AZO)[15], indium zinc oxide (IZO)[16, 17] and fully evaporated molybdenum oxide/gold/molybdenum oxide (MoOx/Au/MoOx)[18] have been shown to fabricate high-performance, relatively stable semi-transparent perovskite solar cells. A hole-selective layer (e.g. MoO_x[11, 13, 14, 16, 17]) or an electron-transport layer (e.g. tin oxide (SnO_2)[10], zinc oxide (ZnO)[15], AZO[2]) is needed to effectively extract charges and often critically to alleviate the sputtering damage to the underlying organic or organic-inorganic layers. A more popular approach using an ultra-thin evaporated metal electrode provides high-efficiency but suffers from long-term stability issues due to moisture diffusion and gold (Au) diffusion at elevated temperature. [19] A Vacuum deposited oxide/metal/oxide, in particular IAI is shown here. It has been previously demonstrated as an electrode though as a bottom electrode directly coated onto flexible plastic substrates for light-emitting diodes[20], organic solar cells[21, 22] and other flexible electronics application[23, 24]. The effect on photovoltaic properties of applying MoO_x/IAI as a top electrode on top of a perovskite solar cell device stack has not been explored. Compared to solution based electrodes, vacuum-based electrodes stand out due to their better transparency versus conductivity, good interfacial contact, homogenous coverage, beneficial room-temperature or low-temperature processing conditions and environmental barrier to moisture and oxygen as well as to the egress of the methylammonium iodide.[2, 14, 15, 25, 26]

Here we report efficient semi-transparent perovskite solar cells using a device stack consisting of glass/FTO/SnO_2/$CH_3NH_3PbI_3$/spiro-OMeTAD/MoO_x/IAI as shown in Figure (1a and 1b). Employing a fully RT processed, top transparent electrode (IAI) with high visible transparency versus conductivity and a polarity-selective sputtering buffer layer (MoO_x), this combination enables us to fabricate efficient perovskite devices with much reduced material usage (total

[a] SPECIFIC, College of Engineering, Swansea University, Bay Campus, Swansea, SA1 8EN.
*zhengfei.wei@swansea.ac.uk; t.m.watson@swansea.ac.uk

Electronic Supplementary Information (ESI) available: [details of any supplementary information available should be included here]. See DOI: 10.1039/x0xx00000x

ARTICLE

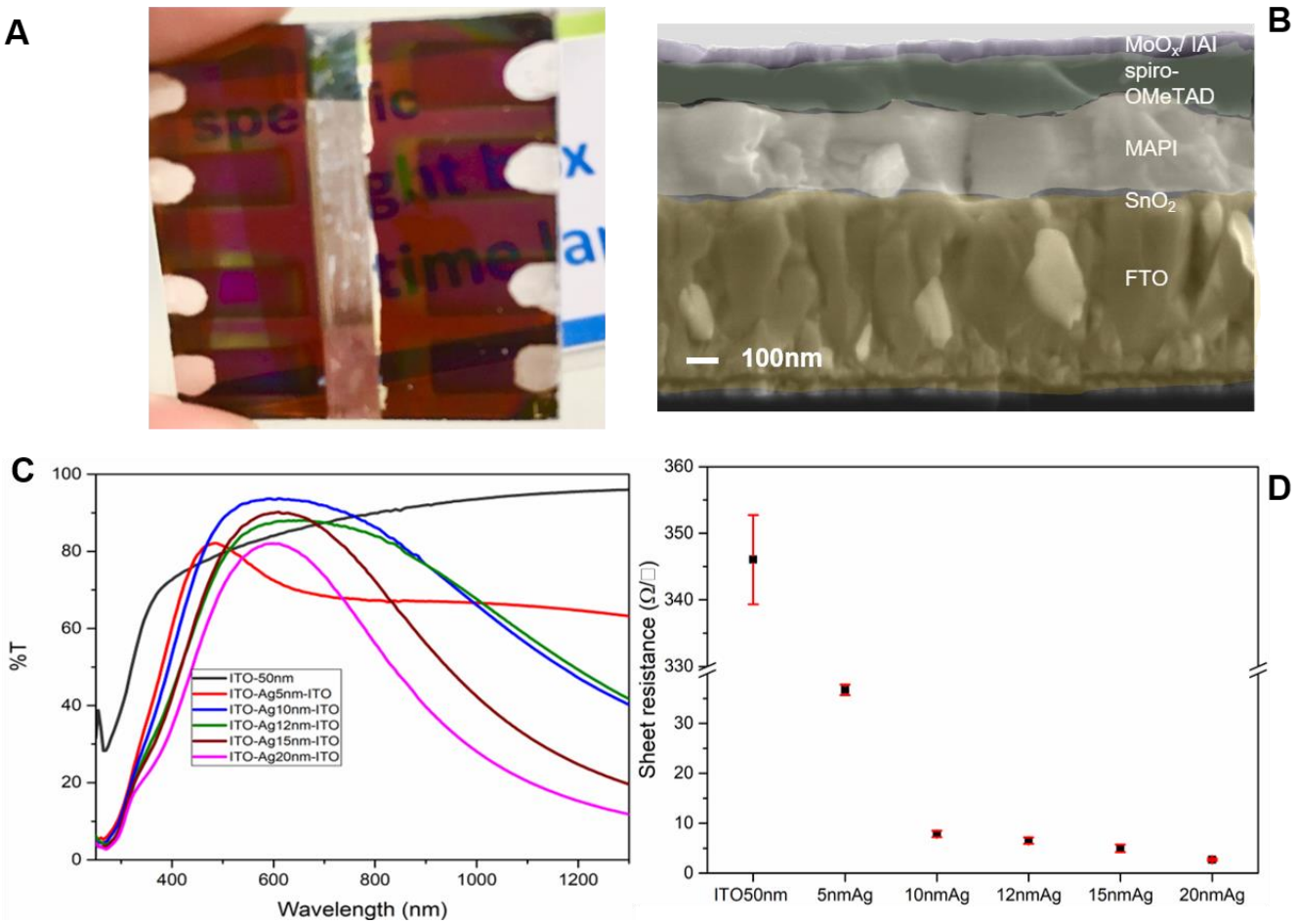

Figure 1. (a) A photograph of a semi-transparent perovskite solar cell. (b) SEM cross-section of the fabricated device. (c) Transmittance of ITO-50 nm and IAI electrodes with different thickness of Ag interlayers in the range of 5-20 nm. (d) The corresponding sheet resistance of IAI electrodes with different thickness of Ag interlayers in the range of 5-20 nm.

thickness of MoO_x/IAI is ~121 nm). The thickness-dependent MoO_x was designed to cover the whole sample area and used here to alleviate the sputtering damage and prevent moisture ingress in combination with the subsequently deposited and patterned IAI electrodes. [2, 14]

Results and discussion

Optical and electrical properties of IAI films

To fabricate semi-transparent devices, IAI transparent electrodes are used here to replace the opaque silver (Ag) electrode. IAI has superior transmittance across the visible to near-infrared (NIR) regions, a filtering effect in the UV region and high conductivity as shown in the Figure 1c. The thickness of ITO was fixed at 50 nm for both top and bottom ITO layers to provide a uniform coverage across the whole substrate. The bottom ITO layer (prepared using low sputtering power to minimise damage) combined with the MoO_x layer provides enough protection for the underlying layers from the subsequent sputtering damage that might be caused by the high energetic ion bombardment during sputtering of the top ITO layer (prepared using high sputtering power to maximise conductivity/transparency and compactness). The thickness of the intermediate Ag layers was varied between 5 nm and 20 nm. 12 nm was found to exhibit best transparency versus conductivity, finest uniformity and highest average transmittance across the wavelength range from 500 nm to

1250 nm. Hence, all the devices made in this work use a 12 nm thick Ag interlayer in the middle of the IAI stack. Although the 50 nm-thick ITO film exhibit high transmittance across the wavelength range from 300-1300 nm (Figure 1c), the sheet resistance of the room-temperature deposited 50 nm-thick ITO using low sputtering power to be used as the bottom layer was measured at 346±6.7 Ω/□ with high non-uniformity across the 2.5 cm x 2.5 cm substrate area (Figure 1d). The high non-uniformity of this layer stems from the growth conditions at low growth temperature, low sputtering power and low film thickness, which has been described using a structure zone diagram (SZD) previously.[27] After coating Ag and the top high-power ITO layers, resistance decreased significantly, furthermore a reduction in data spread suggest greater homogeneity, see Figure 1d. However, the transmittance in the wavelength of UV region (250-400 nm) and NIR (800-1300 nm) of IAI films are lower than 50 nm-ITO (Figure 1c), this is due to scattering of light by Ag islands and high surface roughness, consistent with previous reports.[20, 21, 23] For the IAI electrodes with Ag layers with thickness above 10 nm, a much improved layer coverage is observed with sheet resistance all below 6.5 Ω/□. A complete device (glass/FTO/SnO_2/$CH_3NH_3PbI_3$/spiro-OMeTAD/MoO_x/IAI) with ITO-Ag12nm-ITO top electrode shows a good NIR transmittance and low visible transmittance, this is shown alongside the influence of the MoO_x films in Figure S1. It has been reported the transparency of perovskite solar cells can be further improved by varying the composition and thickness of $MAPbI_{3-x}Br_x$ films.[18]

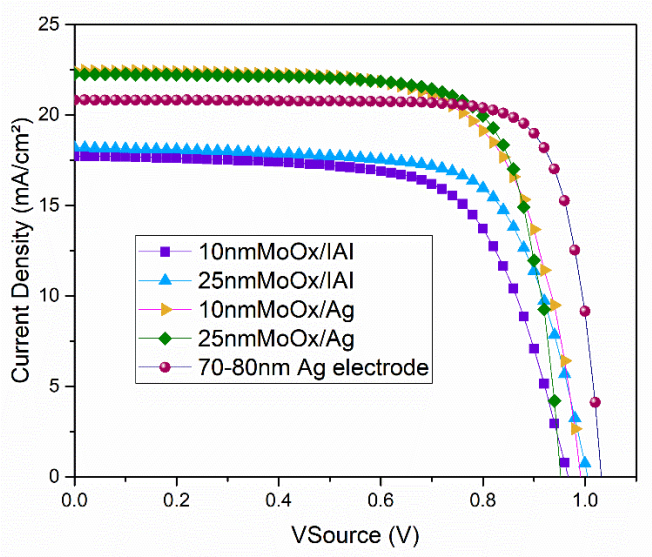

Figure 2. Current density-voltage (J-V) curves of the best-performing perovskite solar cells with opaque Ag electrode (70-80 nm), 10 nm- and 25 nm-MoO_x/opaque Ag electrodes and 10 nm- and 25 nm-MoO_x/IAI electrodes in reverse scan (1.2 V to -0.05V) with a step size of 20 mV and a scan velocity of 175 mVs^{-1}, measured under standard test condition (25 °C, AM1.5G, 1000 Wm^{-2}). The device was pre-light-soaked for 78 s prior to measurements. The cell area was masked to be 0.09 cm^2.

Table 1. Photovoltaic parameters of the best performing perovskite solar cells with different top contact structures.

Devices	η (%)	V_{OC}(V)	J_{SC} (mAcm^{-2})	*FF*	R_S (Ωcm^2)	R_{SH} (Ωcm^2)
Control - Ag	17.41	1.03	20.82	0.81	3.35	67563
10nm MoO_x/Ag	15.39	0.99	22.46	0.69	4.70	4239
25nm MoO_x/Ag	16.27	0.95	22.26	0.77	3.75	12830
10nm MoO_x/IAI	11.54	0.97	17.72	0.67	8.82	2913
25nm MoO_x/IAI	12.86	1.00	18.18	0.70	7.65	2336

Photovoltaic performance

Figure 2 presents the photovoltaic performance of the best performing planar perovskite solar cell with the control opaque Ag electrode, the MoO_x/Ag electrode and the transparent MoO_x/IAI electrode measured under standard test conditions (25 °C AM 1.5G, 1000Wm^{-2}), respectively. It is important to note that the light was illuminated through the FTO side for all devices fabricated in this work in order to avoid the high UV-blue light absorption across the wavelength range from 350 nm to 450 nm.[28, 29] The corresponding main photovoltaic parameters are summarised in Table 1. All the fabricated devices were unencapsulated and the measurements were done in ambient air with a relative humidity of 50% RH. The selection of Ag for the control device is designed to maintain the consistence and direct comparison with MoO_x/Ag and IAI electrodes (the statistics of the device data of samples of MoO_x with thicknesses of 10 nm, 25 nm and 50 nm are presented in supplementary information S1). By introducing 10 nm and 25 nm MoO_x, there is a drop in efficiency mainly due to the reduction of open-circuit voltage (V_{OC}) and fill factor (*FF*) along with slightly boosted short-circuit current (J_{SC}). This could be attributed to the lower conduction band of MoO_x as compared to Ag, which could lead to reduced hole extraction and increased recombination at the interface.[30] Comparing to the device containing Ag only, the reduced efficiency of the devices with the transparent IAI electrode mainly stems from the pronounced loss on J_{SC} and *FF*. For J_{SC}, the higher sheet resistance of IAI compared to Ag would lead to the increase of series resistance (R_S) and loss of J_{SC}. The proportionally varied *FF* and shunt resistance (R_{SH}) of the devices with IAI electrodes are significantly lower than the Ag only and MoO_x/Ag devices, which would indicate a higher leakage current or a partially damaged junction for the MoO_x/IAI based devices. It has been reported that under sputter ion irradiation, the underlying organic material surface becomes damaged and somewhat metallic-like and hence leads to a higher leakage current in the device.[31, 32] Despite a 10 nm or 25 nm MoO_x barrier layer coating, some high-energy sputtering particles are still able to penetrate the weakly bonded MoO_x (possibly due to non-uniformity of underlying layers) and damage the Sprio-OMeTAD and/or perovskite layers. As a consequence this leads to a high leakage current and reduction in R_{SH} for the IAI based devices. A more pronounced hysteresis was also observed for the devices with the transparent IAI top electrode compared with the device

with Ag top electrode as shown in supplementary information Figure S2 and S3. This is possibly caused by the sputtering damage on the n-i-p junction by the high energy sputtered particles.[2, 15]

Device stability

The highest performing devices from each set were kept unencapsulated whilst being exposed to 1 sun illumination for several hours in a light soaking unit (Solaronix Solixon A20), at 25 °C and ambient humidity, and measured every hour to assess their stability. The devices were held at open circuit between scans. All the devices were stored in the dark under standard lab conditions for 5 days before starting the stability measurement. Hence, the starting efficiencies of the chosen devices are slightly lower than the values reported in Table 1.

In Figure 3, the control devices with Ag and MoO_x/Ag electrodes (both 10 nm and 25 nm) have already started to degrade at the beginning of the test i.e. after 5 days of storage in the dark. Under illumination, the efficiencies of these opaque devices drop to below 5% within 10 hours. After 20 hours, they have lost their efficiencies completely. Such a rapid degradation is attributed to reaction between Ag and iodine ions (I^-) from the perovskite layer[33] and fast oxygen diffusion into MAPI films to form photo-induced superoxide species.[25, 26]

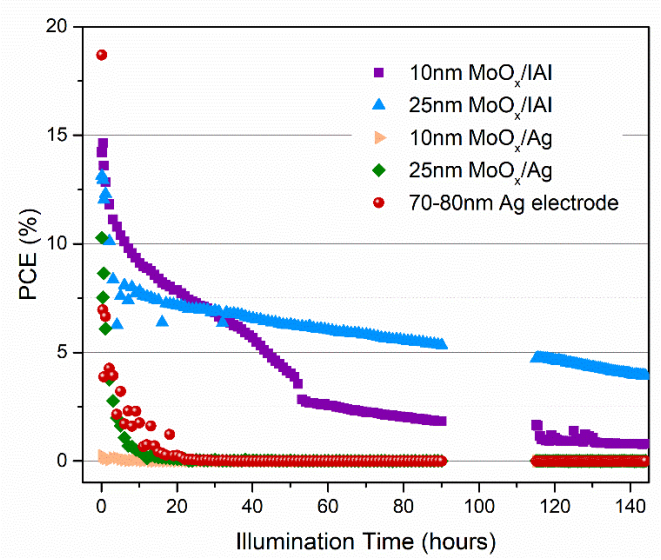

Figure 3. Stability data of the perovskite solar cell devices with the opaque electrode and the semi-transparent IAI electrode. All devices were not encapsulated and kept at open circuit under continuous simulated AM 1.5 illumination at ambient conditions (25°C, 50% RH) and measured every hour. The blank gap between 90 hours and 115 hours is due to an accidental shutdown of the system: during this time the cells were kept under illumination and at open circuit but not measured.

The device with 10 nm MoO_x/IAI semi-transparent electrode shows a slower degradation rate and maintains its efficiency (>5%) for up to 40 hours. Remarkably, the device with 25 nm MoO_x/IAI top electrode presents an even slower degradation rate, keeping efficiency over 5% beyond 90 hours. A much reduced degradation rate for the device with 25 nm MoO_x as compared to the one with 10 nm MoO_x is observed and this may be due to an increase in the distance required to travel by any Ag from the IAI layers or any halogen ions from perovskite diffusing through the bottom low power and likely amorphous ITO. These unwanted ion diffusions and their reactions lead to degradation of the fabricated devices. To be noted, the MoO_x layer was coated covering the whole substrate area while IAI was only coated using a mask and resulting in eight rectangular stripes as shown in Figure 1a. Given the short lifetime reported for the 25nm MoO_x layer without an IAI layer 25nm MoO_x/Ag) there is clearly a combined effect on increasing lifetime derived from both a thicker MoO_x layer and the presence of an ITO coating, despite previous reports of a thicker MoOx decreasing lifetime. [34] In order to illustrate the lifetime enhancement achieved by ITO, XRD analysis was carried out on films with and without ITO layer. Figure 4 shows XRD results on materials formed on both fresh and aged perovskite/spiro-OMeTAD with and without 50 nm thick high-power ITO top layer. Following 8 days of exposure the perovskite/spiro-OMeTAD films without ITO show an additional peak at 28° and much reduced intensity of the peaks at 14.2° and 28.5° signifying degradation. These peaks are not present when ITO has been used as an overlayer. The similar variation on XRD spectra were reported in previous publications.[26, 35] It should be noted that even though an ITO only layer provides appropriate lifetime enhancement it is not possible to fabricate efficient devices due to the sputtering damage on underlaying films including the spiro-OMeTAD. Further evidence on the protective effect of ITO can be found from colour change (RGB) analysis of films (Figure S4).

The stability and XRD data show clearly that is a combination of MoO_x and IAI that is responsible for a reduced degradation rate of the device. The transparent IAI electrode serves as an environmental barrier for oxygen and moisture that channel into the device structure hence the stability of these semi-transparent perovskite solar cells has been improved significantly. The MoO_x with optimised thickness of 25 nm enabled deposition of sputtered ITO layer with reduced under-film damage and serves as an effective barrier to reduce both the unwanted inwards diffusion of Ag from IAI layers outwards diffusion of halogen ions.

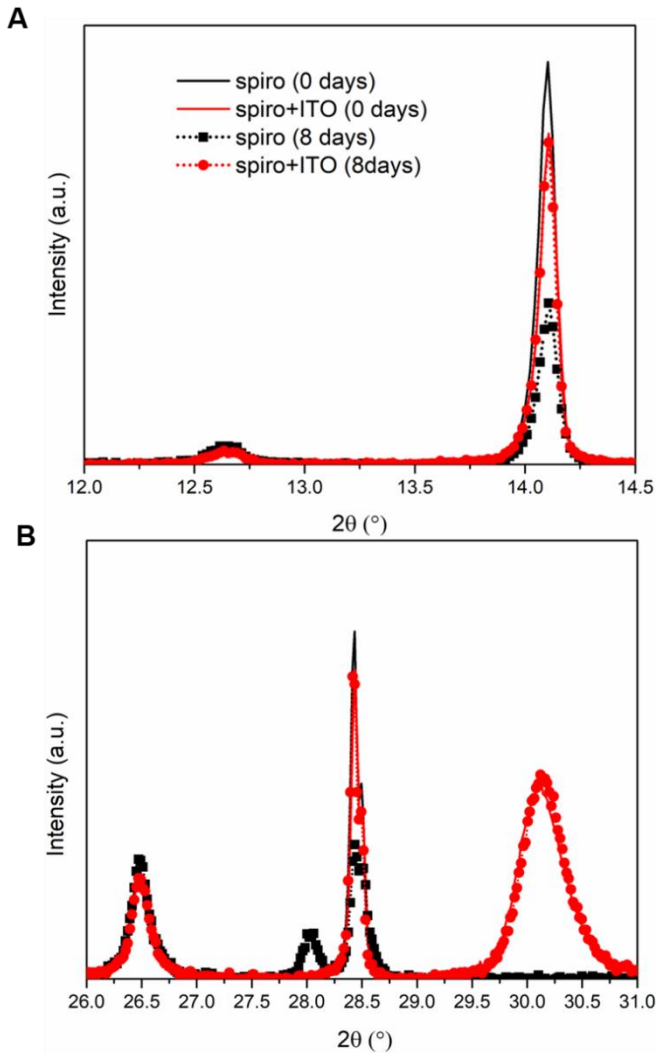

Figure 4. XRD data of perovskite/spiro-OMeTAD films with and without ITO coating before and after 8 days of illumination at 3580 lux in the light box used for the time lapse photography and RGB analysis. The light spectrum and experimental set up could be found in a previous publication. [36]

Conclusions

In conclusion, we have demonstrated a 12.85% efficiency semi-transparent planar perovskite solar cell using the transparent MoO_x/IAI based top electrode. MoOx is used here to allow the deposition of IAI directly on to the device stack providing increased conductivity and transparency. Furthermore, this electrode served as an effective environmental barrier to oxygen and moisture and hence it improved the stability of this type of device significantly. This work shows the promising prospect of integrating semi-transparent perovskite solar cells into future window applications and tandem devices.

Experimental

Top Electrode Preparation: The molybdenum oxide (MoO_x, STREM, 99.95%) and silver (Ag, Kurt Leskar, 99.99%) films were thermally evaporated using a MBRAUN evaporator with evaporation rate of 0.5 Å s^{-1} and 0.25 Å s^{-1}, respectively. The indium and tin oxide target (ITO target, Plasmaterial 99.99%) films were RF magnetron sputtered using a Moorfield Nanolab 60 sputtering system at 0.37 Wcm^{-2} and 2.06 Wcm^{-2} for the bottom and top layers.

Perovskite Solar Cell Fabrication

Pilkington TEC15 TM (<15 Ωcm^{-2}) glass was first gently scrubbed with a concentrated solution of Hellmanex® III (10% by volume) diluted in de-ionised water and rinsed with copious amounts of de-ionised water. Substrates were then submerged and sonicated in a 2 % by volume Hellmanex solution diluted in de-ionised water (~18 mΩ) at 80 °C for 20 minutes. After this time, the substrates were removed and rinsed with more de-ionised water and placed into a bath of de-ionised water (only) and sonicated for a further 20 minutes at 80 °C to remove any residual surfactant. After this the substrates were subsequently rinsed with copious amounts of de-ionised water, acetone, ethanol and isopropanol. The substrates were then blown dry with a nitrogen air knife and placed into an oxygen plasma cleaner for 15 minutes on full power to remove any residual carbon contaminants and make the surfaces more hydrophilic. Lastly samples were placed in UV-Ozone chamber for 15 minutes to aid with improved wettability and film formation for the subsequent SnO_2 layer. Substrate preparation was carried out in a validated class 1000 clean room.

SnO_2 ETL layers were prepared by diluting (44592) Tin (IV) oxide, 15% in H_2O colloidal dispersion procured from Alfa Aesar further in de-ionised water to the ratio 1: 2.6 ml to give a final solution of 4.2 wt.%. These were then deposited via spin coating immediately after UV-Ozone treatment of the FTO was finished. We note that the increased wetting effects of UV-Ozone on FTO films lasts no longer than 10 minutes, we found it imperative that films were spin coated before this time limit elapsed. 150 µl of the final ETL solution was spin coated onto a 28 mm by 28 mm glass/ FTO substrate at 2000 rpm / 2000$rpms^{-1}$ for 30 s, we noted improved surface coverage by depositing the solution dynamically at 25 s. The substrates were then placed on a hotplate at 110 °C for 10 minutes then a 5-minute ramp to 180 °C for 1 hour to anneal the final films. We note that processing conditions in the laboratory are critical to good film formation, noting that a very dry room (<25 % RH) coupled with a nitrogen flowed Laurel (Model: WS-650Mz-23NPPB spin processor) spin coater contributed to rapid drying of the film, resulting in detrimental pin hole defects. Increased humidity of >30% RH and no nitrogen flowing in the spin coater resulted in more homogenous films. These conditions should be considered when trying to fabricate such a layer as the effects can be easily negated although are not obvious during manufacture. procedure was carried out in nitrogen filled glove-box.

MAPI perovskite was prepared by dissolving 605 mg of Lead Iodide (PbI_2) procured from TCI America and 199 mg of methylammonium iodide (MAI) procured from GreatCellSolar in 1 ml of 4:1 ratio of Dimethylformamide: Dimethyl Sulfoxide. We noted that by dissolving the inorganic PbI2 at elevated

temperatures >150 °C resulted in better perovskite film formation with fewer pinholes as report in literature.1 The solution was then filtered using a 0.2 µm PTFE filter and deposited on top of the SnO_2 via solution processed spin coating (125 µL, 4000 rpm/ 2000 $rpms^{-1}$ for 30 s). During the spin coating process, 200 µL of ethyl acetate procured from Sigma Aldrich was deposited dynamically onto the spinning substrate 22 s before the end the second spin programme. Once the spin coating procedure had finished the films were transferred to a hotplate and annealed at 100 °C for 1 hour. The entire perovskite procedure was carried out in nitrogen filled glove-box.

For the hole trans- porting material (HTM), a Spiro-OMeTAD solution (100 mg of Spiro-OMeTAD, 36 µL of 4-tert-butylpyridine (tBP), 20 µL of a lithium-bis(tri-fluoromethanesulfonyl)imide (Li- TFSI) solution (516 mg Li-TFSI in 1 mL acetonitrile) and 8 µL of a FK209 (300 mg in 1 mL of acetonitrile) in 996 µL of chlorobenzene) was spin-coated dynamically at 4000 rpm, 4000 $rpms^{-1}$ for 12 s on top of the annealed perovskite. Again, the preparation and deposition of the HTM was performed in a nitrogen filled glove-box. Finally, 70-80 nm of Ag top electrode was thermally evaporated under high vacuum.

Characterisation: The morphology of films was studied using a JEOL-JSM-7800F field emission scanning electron microscope (5 kV acceleration voltage, a working distance of 10 mm and a magnification of x 50, 000). The transmittance of the IAI films were scanned suing a PerkinElmer Lambda 750 UV/VIS/NIR Spectrometer. The sheet resistance of the IAI films were measured using a Jandel RM3000 four-point probe station. X-ray diffraction data were collected on a D8 Discover (Bruker) X-ray diffractometer operating at 40 kV and 40 mA. Scans were collected between 10 and 60 degree with a 0.02 degree step.

For current-voltage measurements of solar celldevices were masked to 0.09 cm^2 and tested under a class AAA solar simulator (Newport Oriel Sol3A) at AM1.5 and 100 $mWcm^{-2}$ illumination conditions calibrated against a KG5 filtered silicon reference cell (Newport Oriel 91150-KG5) using a Keithley 2400 source meter. Current-voltage sweeps were performed from both V_{OC} to J_{SC} and vice versa at a rate of 0.1 Vs^{-1}. For stabilized power output measurements, device bias was set to the maximum power point voltage determined by the J-V sweep and current monitored under 1000 Wm^{-2} illumination.

Stability measurements were performed on unencapsulated devices kept at open circuit in a light soaking unit (Solaronix Solixon A20), at 25 °C and ambient humidity, under 1 sun illumination: both reverse and forward scans, at 15mV/s scan rate, were carried at every hour. The time lapse photography and RGB analysis to assess the colour change of the different films and thus their degradation over time were carried out as in our previous work.[36]

Conflicts of interest

There are no conflicts to declare.

Acknowledgements

The IMPACT operation has been part-funded by the European Regional Development Fund through the Welsh Government and Swansea University. The authors would also like to thank the Engineering and Physical Sciences Research Council (EPSRC) through the SPECIFIC Innovation and Knowledge centre Phase 2 (EP/ N020863/1). The Authors would also like to express their gratitude to the Welsh Government for their support of the Sêr Solar programme. The IMPACT operation has been part-funded by the European Regional Development Fund through the Welsh Government and Swansea University. This work has been supported by the European Social Fund (ESF) through the Welsh Government (80339); EPSRC (EP/K503228/1); Swansea University EPSRC impact acceleration account and the COATED doctoral training centre, Materials and Manufacturing Centre (M2A), Swansea University College of Engineering.

Notes and references

1. M. A. Green, Y. Hishikawa, E. D. Dunlop, D. H. Levi, J. Hohl-Ebinger and A. W. Y. Ho-Baillie, *Progress in Photovoltaics: Research and Applications*, 2018, **26**, 427-436.
2. K. A. Bush, C. D. Bailie, Y. Chen, A. R. Bowring, W. Wang, W. Ma, T. Leijtens, F. Moghadam and M. D. McGehee, *Advanced Materials*, 2016, **28**, 3937-3943.
3. C. D. Bailie, M. G. Christoforo, J. P. Mailoa, A. R. Bowring, E. L. Unger, W. H. Nguyen, J. Burschka, N. Pellet, J. Z. Lee, M. Grätzel, R. Noufi, T. Buonassisi, A. Salleo and M. D. McGehee, *Energy & Environmental Science*, 2015, **8**, 956-963.
4. C. O. Ramírez Quiroz, Y. Shen, M. Salvador, K. Forberich, N. Schrenker, G. D. Spyropoulos, T. Heumüller, B. Wilkinson, T. Kirchartz, E. Spiecker, P. J. Verlinden, X. Zhang, M. A. Green, A. Ho-Baillie and C. J. Brabec, *Journal of Materials Chemistry A*, 2018, **6**, 3583-3592.
5. M. Xie, H. Lu, L. Zhang, J. Wang, Q. Luo, J. Lin, L. Ba, H. Liu, W. Shen, L. Shi and C.-Q. Ma, *Solar RRL*, 2018, **2**, 1700184.
6. Z. Li, S. A. Kulkarni, P. P. Boix, E. Shi, A. Cao, K. Fu, S. K. Batabyal, J. Zhang, Q. Xiong, L. H. Wong, N. Mathews and S. G. Mhaisalkar, *ACS Nano*, 2014, **8**, 6797-6804.
7. F. Jiang, T. Liu, S. Zeng, Q. Zhao, X. Min, Z. Li, J. Tong, W. Meng, S. Xiong and Y. Zhou, *Opt. Express*, 2015, **23**, A83-A91.
8. P. You, Z. Liu, Q. Tai, S. Liu and F. Yan, *Advanced Materials*, 2015, **27**, 3632-3638.
9. J. Troughton, D. Bryant, K. Wojciechowski, M. J. Carnie, H. Snaith, D. A. Worsley and T. M. Watson, *Journal of Materials Chemistry A*, 2015, **3**, 9141-9145.
10. K. A. Bush, A. F. Palmstrom, Z. J. Yu, M. Boccard, R. Cheacharoen, J. P. Mailoa, D. P. McMeekin, R. L. Z. Hoye, C. D. Bailie, T. Leijtens, I. M. Peters, M. C. Minichetti, N. Rolston, R. Prasanna, S. Sofia, D. Harwood, W. Ma, F. Moghadam, H. J. Snaith, T. Buonassisi, Z. C. Holman, S. F. Bent and M. D. McGehee, *Nature Energy*, 2017, **2**, 17009.
11. P. Löper, S.-J. Moon, S. Martín de Nicolas, B. Niesen, M. Ledinsky, S. Nicolay, J. Bailat, J.-H. Yum, S. De Wolf and C.

Ballif, *Physical Chemistry Chemical Physics*, 2015, **17**, 1619-1629.
12. M. Jaysankar, W. Qiu, M. van Eerden, T. Aernouts, R. Gehlhaar, M. Debucquoy, U. W. Paetzold and J. Poortmans, *Advanced Energy Materials*, 2017, **7**, 1602807.
13. T. Duong, Y. Wu, H. Shen, J. Peng, X. Fu, D. Jacobs, E.-C. Wang, T. C. Kho, K. C. Fong, M. Stocks, E. Franklin, A. Blakers, N. Zin, K. McIntosh, W. Li, Y.-B. Cheng, T. P. White, K. Weber and K. Catchpole, *Advanced Energy Materials*, 2017, **7**, 1700228.
14. F. Fu, T. Feurer, T. Jäger, E. Avancini, B. Bissig, S. Yoon, S. Buecheler and A. N. Tiwari, *Nature Communications*, 2015, **6**, 8932.
15. F. Fu, T. Feurer, Thomas P. Weiss, S. Pisoni, E. Avancini, C. Andres, S. Buecheler and Ayodhya N. Tiwari, *Nature Energy*, 2016, **2**, 16190.
16. J. Werner, G. Dubuis, A. Walter, P. Löper, S.-J. Moon, S. Nicolay, M. Morales-Masis, S. De Wolf, B. Niesen and C. Ballif, *Solar Energy Materials and Solar Cells*, 2015, **141**, 407-413.
17. H. Shen, T. Duong, J. Peng, D. Jacobs, N. Wu, J. Gong, Y. Wu, S. K. Karuturi, X. Fu, K. Weber, X. Xiao, T. P. White and K. Catchpole, *Energy & Environmental Science*, 2018, **11**, 394-406.
18. L. Yuan, Z. Wang, R. Duan, P. Huang, K. Zhang, Q. Chen, N. K. Allam, Y. Zhou, B. Song and Y. Li, *Journal of Materials Chemistry A*, 2018, **6**, 19696-19702.
19. B. Chen, Y. Bai, Z. Yu, T. Li, X. Zheng, Q. Dong, L. Shen, M. Boccard, A. Gruverman, Z. Holman and J. Huang, *Advanced Energy Materials*, 2016, **6**, 1601128.
20. S.-M. Lee, H.-W. Koo, T.-W. Kim and H.-K. Kim, *Surface and Coatings Technology*, 2018, **343**, 115-120.
21. J.-A. Jeong and H.-K. Kim, *Solar Energy Materials and Solar Cells*, 2009, **93**, 1801-1809.
22. J. H. Kim, T.-W. Kang, S.-N. Kwon, S.-I. Na, Y.-Z. Yoo, H.-S. Im and T.-Y. Seong, *Journal of Electronic Materials*, 2017, **46**, 306-311.
23. N. Ren, J. Zhu and S. Ban, *AIP Advances*, 2017, **7**, 055009.
24. K. P. Sibin, G. Srinivas, H. D. Shashikala, A. Dey, N. Sridhara, A. Kumar Sharma and H. C. Barshilia, *Solar Energy Materials and Solar Cells*, 2017, **172**, 277-284.
25. D. Bryant, N. Aristidou, S. Pont, I. Sanchez-Molina, T. Chotchunangatchaval, S. Wheeler, J. R. Durrant and S. A. Haque, *Energy & Environmental Science*, 2016, **9**, 1655-1660.
26. N. Aristidou, C. Eames, I. Sanchez-Molina, X. Bu, J. Kosco, M. S. Islam and S. A. Haque, *Nature Communications*, 2017, **8**, 15218.
27. A. Anders, *Thin Solid Films*, 2010, **518**, 4087-4090.
28. S. Fantacci, F. De Angelis, M. K. Nazeeruddin and M. Grätzel, *The Journal of Physical Chemistry C*, 2011, **115**, 23126-23133.
29. T. Krishnamoorthy, F. Kunwu, P. P. Boix, H. Li, T. M. Koh, W. L. Leong, S. Powar, A. Grimsdale, M. Grätzel, N. Mathews and S. G. Mhaisalkar, *Journal of Materials Chemistry A*, 2014, **2**, 6305-6309.
30. T. Duong, N. Lal, D. Grant, D. Jacobs, P. Zheng, S. Rahman, H. Shen, M. Stocks, A. Blakers, K. Weber, T. P. White and K. R. Catchpole, *IEEE Journal of Photovoltaics*, 2016, **6**, 679-687.
31. L.-S. Hung and J. Madathil, *Thin Solid Films*, 2002, **410**, 101-106.
32. L. S. Liao, L. S. Hung, W. C. Chan, X. M. Ding, T. K. Sham, I. Bello, C. S. Lee and S. T. Lee, *Applied Physics Letters*, 1999, **75**, 1619-1621.
33. Y. Kato, L. K. Ono, M. V. Lee, S. Wang, S. R. Raga and Y. Qi, *Advanced Materials Interfaces*, 2015, **2**, 1500195.
34. E. M. Sanehira, B. J. Tremolet de Villers, P. Schulz, M. O. Reese, S. Ferrere, K. Zhu, L. Y. Lin, J. J. Berry and J. M. Luther, *ACS Energy Letters*, 2016, **1**, 38-45.
35. N. Aristidou, I. Sanchez-Molina, T. Chotchuangchutchaval, M. Brown, L. Martinez, T. Rath and S. A. Haque, *Angewandte Chemie International Edition*, 2015, **54**, 8208-8212.
36. T. J. Wilderspin, F. De Rossi and T. M. Watson, *Solar Energy*, 2016, **139**, 426-432.

Graphic Abstract